Offshore sea levels measured with an anchored spar-buoy system using GPS interferometric reflectometry

Surui Xie[1], Jing Chen[2], Timothy H. Dixon[3], Robert H. Weisberg[2], Mark A. Zumberge[1]

[1]Scripps Institution of Oceanography, University of California, San Diego, La Jolla, CA, USA.

[2]College of Marine Science, University of South Florida, St. Petersburg, FL, USA.

[3]School of Geosciences, University of South Florida, Tampa, FL, USA.

Correspondence to: Surui Xie (suxie@ucsd.edu)

Key Points:

- An anchored spar-buoy seafloor geodetic system is used to measure offshore sea levels based on GPS interferometric reflectometry (GPS-IR).
- Agreement of daily mean sea levels measured by the GPS spar-buoy and a nearby acoustic tide gauge is 3.1 cm.
- Sea levels measured with the GPS spar-buoy can help improve coastal ocean circulation models.

Abstract

Conventional tide gauges are usually housed along the coast. Satellite altimetry works well in the open ocean but poorly near the coast due to issues such as signal contamination by land returns. These limitations lead to an observational gap in the coastal ocean. Using data collected by a GPS installed on top of an anchored spar-buoy in Tampa Bay, we retrieved water levels through a combination of precise positioning and interferometric reflectometry. Individual water level retrievals agree with a nearby acoustic tide gauge at ~16 cm level. Amplitude and phase of the major tidal constituents are well recovered by the GPS spar-buoy measurements. Over a 2-year period, agreement of daily mean sea levels measured by the GPS spar-buoy and a nearby acoustic tide gauge is 3.1 cm. When sea level data measured by the GPS spar-buoy are included in the coastal ocean circulation model, low-frequency error propagated from the open boundary is reduced.

Plain Language Summary

GPS receivers record direct signals from satellites as well as reflected signals from local objects. The reflected signals can interfere with the direct signals, enhancing or reducing overall signal strength. This characteristic can be used to measure the height difference between the GPS antenna and the reflecting surface. We used GPS data collected by a spar-buoy anchored in Tampa Bay to calculate water levels at different times. The calculated water levels can be used to study sea level change, ocean circulation, and tidal height predictions.

Keywords

Sea level; GPS spar-buoy; interferometric reflectometry; tide gauge; coastal ocean model; Tampa Bay.

1 Introduction

Global navigation satellite systems (GNSS), including the Global Positioning System (GPS), have been widely used in Earth science studies, such as crustal deformation (e.g., Dixon, 1991), atmospheric water vapor variation (e.g., Bevis et al., 1992), ionosphere perturbation (e.g., Ho et al., 1996), tide gauge calibration (Watson et al., 2008), ice motion (Zhang et al., 2008), and volcanic plume detection (Larson, 2013). One of the error sources for precise positioning, multipath, can be used to measure the height and other characteristics of the reflecting surface using a technique called interferometric reflectometry (Larson et al., 2013, 2017, 2021; Larson & Nievinski, 2013; Liu & Larson, 2018; Roesler & Larson, 2018; Peng, 2019; Karegar et al., 2020; Purnell et al., 2020; Wang et al, 2020). GNSS interferometric reflectometry (GNSS-IR) exploits the periodic constructive and destructive interference between the direct and the reflected signals. The resulting oscillation in signal-to-noise ratio (SNR) can be used to estimate the height difference between the phase center of the GNSS antenna and the reflecting surface (Larson & Nievinski, 2013). Among different reflectors, water is a nearly specular reflector and is well-suited to GNSS-IR applications. Previous studies demonstrated typical root-mean-square (RMS) differences between water levels measured by ground-based GNSS-IR and conventional tide gauges on the order of ~10 cm for individual estimates and a few centimeters for daily means (e.g., Williams & Nievinski, 2017; Larson et al., 2017; Peng et al., 2019). When the antenna is in

kinematic mode, i.e., mounted on a moving platform, water level estimates by GNSS-IR become noisier due to the platform's complicated motion (e.g., Roggenbuck & Reinking, 2019).

Compared to conventional tide gauges (e.g., acoustic sounding tube, radar or pressure sensors), the sampling rate and corresponding precision for GNSS-IR is lower. However, this technique has several advantages over conventional tide gauges. For example, GNSS-IR can measure absolute water level changes without relying on additional data such as vertical land motion, and the hardware needs little maintenance. Considering that there are many geodetic quality GNSS stations available, and for most of them the primary purpose is precise positioning, GNSS-IR can provide useful sea level measurements without additional cost.

While water level measurements with GNSS-IR have been demonstrated in a number of studies, previous applications are mainly in coastal areas with stationary GNSS sites (e.g., Larson et al., 2013, 2017, 2021; Peng et al., 2019). Roggenbuck & Reinking (2019) tested the method with three months of data collected by a ship-based GNSS antenna along a ferry route. The standard deviation of the differences between the estimated water levels and a nearby tide gauge measurements in that study was about 4-6 cm. Here we use a GPS station installed on an anchored spar-buoy to measure offshore water levels at a fixed site (Figure 1). The system was designed for measuring three-component seafloor motion, with the GPS antenna placed on top of the spar, and the bottom of the spar connected to a heavy ballast by a shackle. A float is integrated into the spar to provide buoyancy, keeping the buoy near vertical (Xie et al., 2019). The GPS antenna is constantly moving due to strong tidal currents and other environmental forcing, representing a potential noise source. Height changes of the antenna above water are caused by a combination of vertical motion of the anchor, spar tilt, and water level changes,

although after several months of settling vertical motion of the anchor is minimal. Since only GPS data are used in this study, we refer to the method as GPS-IR unless noted.

2 GPS Data

Dual-frequency (L1 and L2) GPS data obtained between 23 August 2018 and 15 September 2020 were used in this study. In different experimental stages, the data sampling intervals differ: 15-second from 23 August 2018 to 17 May 2019, 5-second from 18 May 2019 to 25 August 2019, and 30-second from 26 August 2019 to 15 September 2020. A satellite elevation angle mask of 7º was set in the receiver. SNR data collected when the satellite elevation angle was between 7º and 13º were used in the GPS-IR analysis. Figure 1b shows an example of GPS-signal multipath reflection points. Figure 1c shows an example of the sensing zones on water (First Fresnel Zones, see details in Larson & Nievinski (2013)) for satellites at 7º and 13º elevation angles. The gap in the north direction is due to orbit limitations in the satellite constellation. Compared to many coastal GNSS sites where some of the sensing zones are not on water or are obstructed, in our case data collected from all directions can be used.

Note that some previous GNSS-IR studies used SNR data collected at lower satellite elevation angles (e.g., Larson et al., 2013; Peng et al., 2019; Roggenbuck & Reinking, 2019). However, in our case the GPS spar-buoy system was not originally designed for GPS-IR measurements, hence a 7º elevation angle mask was used to reduce multipath noise in precise positioning and limit data rate. A maximum elevation angle of 13º was chosen because the effects of multipath modulation on SNR data become less obvious at higher elevation angles. Nevertheless, a satellite track from 7º to 13º provides enough data for reflecting height estimates

(see below). Figure 2a shows a typical one-day example of satellite tracks used for our GPS-IR measurements.

3 Data analysis

Water levels were calculated by $H=H_g-H_r$, where H, H_g, and H_r denote water level, elevation of the GPS antenna phase center, and reflecting height (vertical distance between GPS antenna phase center and the water surface), respectively. Kinematic GPS processing to estimate H_g was reported in Xie et al. (2019); we follow the same method here. Typical formal error of H_g for a single epoch is 4-5 cm. Grey dots in Figure 3a shows the time series of H_g. An exponential subsidence signal is evident, mainly due to anchor settling and tidal current scouring. The total vertical displacement of the buoy is about -0.8 m during the study period.

To estimate the reflecting height H_r, the method described in Larson et al. (2013) was used, with several changes to account for the motion of the GPS antenna, described in the following steps:

1) Data selection: L1 or L2 data obtained during GPS satellite ascending or descending tracks (7^o-13^o elevation angle) were analyzed separately. The average satellite transit time of each track is 18.3 minutes during the study period.

2) Data detrending: A third-order polynomial was used to detrend the SNR versus sin E data, where E represents the GPS satellite elevation angle. This removes long-period variations due to changes in the receiver-satellite distance and the gain pattern of the antenna, leaving the multipath effect (red line in Figure 2b).

3) Preliminary reflecting height estimate: The dominant frequency of the detrended SNR versus sin E data was picked by a Lomb-Scargle periodogram (LSP) analysis, which can be converted to preliminary reflecting height using $H_r=\square*f_{max}/2$, where $\square$ is the wavelength of the GPS signal (19.05 cm for L1, 24.45 cm for L2) and f_{max} is the dominant frequency picked by the LSP analysis (Figure 2c).

4) Nonstationary reflecting height correction: Due to tidal variation and buoy motion, the vertical distance between the antenna and water surface is not constant during each analyzed satellite track, biasing the preliminary reflecting height estimate by $\dot{H}_r \tan E/\dot{E}$ (Larson et al., 2013). An eighth-order polynomial was used to fit a 3-day time series of H_r, and the derivations of the middle day were used for corrections.

Several criteria were used for quality control. First, an iterative method was applied to ensure that only satellite tracks with observation numbers above the Nyquist sampling limit are used. For example, a preliminary analysis shows that the reflecting heights are between 7-11 m during the entire study period, hence a theoretical maximum height of 11.5 m (in a conservative sense) was used to calculate the equivalent frequency and required minimum number of observations to recover the dominant frequency in the subsequent LSP analysis. Second, to ensure the LSP result is robust, the theoretical number of cycles in the SNR versus sin E must be larger than 3. For example, the satellite track shown in Figure 2b has ~5 cycles. Third, to determine if the dominant frequency signal estimated by the LSP analysis is significant, the SNR versus sin E data were detrended by a best fitting sine function (black line in Figure 2b) with the estimated dominant component, and another LSP analysis was applied to the residuals

(periodogram shown by grey line in Figure 2c). If the peak LSP amplitude is reduced by less than 50% between the two LSP analyses, the result is discarded.

GPS microwave signals are subject to tropospheric delays, and previous work suggests they could perceptibly affect GPS-IR measurements (Williams & Nievinski, 2017). We adopted the correction method developed by Williams & Nievinski (2017) and used the discrete products of the Vienna Mapping Functions 3 (VMF3) and the Global Pressure and Temperature 3 (GPT3) model (Landskron & Böhm, 2018) to calculate the tropospheric delays. While the absolute biases due to tropospheric delays in our GPS-IR reflecting height estimates have a mean of 4.0 cm, the fluctuation is small, with a standard deviation of 0.4 cm, primarily due to the relatively small tidal range at the study area (~1 m).

Water levels were calculated by subtracting the GPS-IR-measured reflecting heights from GPS-measured antenna phase center elevations. Since both GPS L1 and L2 signals were used, we combined them to form the final water level product. For each satellite track, if both L1 and L2 data retrieve a water level successfully, then an average value was used in the water level product. Red dots in Figure 3a show the final water level time series measured by the GPS spar-buoy. Compared to data recorded at an acoustic tide gauge 19.5 km away (Figure 1a), the standard deviation of water level differences is 15.7 cm.

4 Discussion

During the study period, an average of 61 water levels per day were retrieved by GPS-IR measurements. While the precision of a single water level estimate by the GPS spar-buoy is much worse than a typical conventional tide gauge [Míguez et al., 2012], it does provide an

independent method for sea level monitoring. Below we discuss quality and potential applications of the water level product derived from the GPS data.

4.1 Factors affecting the precision of water levels measured by the GPS spar-buoy

Water levels (Red dots in Figure 3a) were calculated by subtracting the GPS-IR measured reflecting heights (black dots in Figure 3a) from GPS measured antenna phase center elevations (grey dots in Figure 3a). Since the reflecting height estimates are based on LSP analyses of data obtained at different satellite elevation angles, they should be treated as local averages over the corresponding periods (18.3 minutes on average). Several factors affect the precision of our water level product, discussed below:

1) Vertical motion of the GPS antenna. Unlike stationary sites on land, the GPS antenna on top of the spar-buoy is constantly moving due to wind and tidal currents. Our previous study (Xie et al., 2019) shows that in days without extreme weather events, the buoy moves smoothly within a short period (e.g., several minutes). Hence the nonstationary reflecting height correction works well to address the combined effect of GPS antenna motion and water level change over the satellite tracking period. In contrast, during extreme weather events, bobbing of the buoy reduces the periodicity of the SNR versus sin E relation, worsening the precision of the dominant frequency identified by LSP analysis. Reducing the spar-buoy cross section or increasing the net buoyancy are possible methods to reduce the influence of buoy bobbing on GPS-IR water level measurements.

2) Sea state. During the study period, a number of extreme weather events occurred at the spar-buoy site (Xie et al., 2019). Sea state not only affects the GPS antenna motion, but also

191 directly influences the roughness of the reflecting surface. Previous applications of storm surge
192 detections show that high winds downgrade the performance of GNSS-IR (Peng et al., 2019;
193 Larson et al., 2021). In our case, during extreme weather events (e.g., hurricanes) fewer satellite
194 tracks fulfilled the quality control and the uncertainty in the sea level estimate is larger compared
195 to days with calm sea state (Figure 3b). On the other hand, this suggests that the system could
196 also be used in the future to measure sea state.

197 3) GPS data interval. While a Nyquist sampling limit was used for quality control, this
198 criterion only ensures there is just enough observations to estimate a theoretical dominant
199 frequency in LSP analysis. Denser observations allow more precise reflecting height estimates.
200 Figure 3b-3d compares three 1-month water levels retrievals with different GPS data intervals.
201 Higher rate data lead to higher precision (less scatter) in estimated water levels.

202

203 4.2 Comparison to conventional tide gauge data

204 Compared to a conventional coastal tide gauge located 19.5 km away, precision of water
205 levels measured by the GPS spar-buoy is lower. However, our technique captures both low (cyan
206 lines in Figure 3a) and high (Figure 3b-3d) frequency signals well. Figure 4a-4c shows tidal
207 harmonic analyses of time series obtained from the two techniques. For the eleven largest tidal
208 constituents, the largest amplitude difference is 1.5 cm. Comparing amplitudes, the differences at
209 the two locations are all smaller than 15% except for the tidal constituent S1, which has a period
210 of 24 hr that is also the daily environmental variation cycle. Comparing phases, analyzed tidal
211 constituents at the tide gauge all lag behind the spar-buoy site (Figure 4a). Except for the solar

annual term that has a very long period (8766.2 hr), the other five largest tidal constituents have a mean time lag of 1.5±0.2 hr.

Apart from measurement error in the two techniques, the amplitude and phase differences likely reflect true tidal differences at the two locations given the 19.5 km separation. Figure 5 compares the phases and amplitudes of the three largest tidal constituents (M2, K1, O1) derived from the tide gauge measurements, the GPS spar-buoy measurements, and a widely used ocean tide model OSU TPXO (Egbert & Erofeeva, 2002). For the phase or phase differences, the GPS spar-buoy and tide gauge data yield results similar to the ocean tide model (Figure 5a-5c). For the tidal amplitudes, even though the GPS spar-buoy and tide gauge-derived values are systematically smaller than the ocean tide model, both data and model suggest that the amplitude differences of the largest three tidal constituents at the two locations is just a few centimeters.

Figure 4d-4e shows a comparison of tide gauge-observed water levels and predictions from different data sources. The tidal ranges predicted from the GPS spar-buoy or tide gauge data match well with the various observations. However, the OSU TPXO model-predicted tidal ranges at the tide gauge or spar-buoy location are both larger than the observations (Figure 4d-4f). We interpret the apparently larger tidal amplitude as an error in this coastal region for the ocean tide model, since the major data source of the OSU TPXO model is satellite altimetry (TOPEX/Poseidon), which has poor performance near coasts mainly due to contamination of the pulse-limited radar altimeter footprints from land returns (Tamisiea et al., 2014).

To assess the ability of the GPS spar-buoy to monitor sea level change, we subtracted the water level variability due to constituent tides (de-tiding). Figure 6a shows the daily means of de-tided water levels measured by the GPS spar-buoy and the tide gauge. The two results correlate well. The RMS of the differences is 3.1 cm, 0.8 cm larger than the RMS of water level

235 differences measured by a stationary land GPS and a nearby tide gauge in Kachemak Bay,
236 Alaska (Larson et al., 2013).

237

238 4.3 Contribution with a coastal ocean model

239 Tampa Bay is the largest of the Florida coastal plain estuaries. With spatial resolution as
240 fine as 20 m, the Tampa Bay Coastal Ocean Model (TBCOM) resolves the channels, inlets,
241 bridge causeways, and other geometric complexities (Chen et al., 2018). To maintain high
242 resolution within the estuary and properly account for exchanges between the continental shelf
243 and estuary, TBCOM downscales from the continental shelf to the estuary by nesting the
244 unstructured grid of the Finite Volume Community Ocean Model (FVCOM) (Chen et al., 2003)
245 in the West Florida Coastal Ocean Model (WFCOM) (Zheng & Weisberg, 2012; Weisberg et al.,
246 2014), which in turn downscales from the deep ocean, across the continental shelf by nesting
247 FVCOM in the Gulf of Mexico Hybrid Coordinate Ocean Model (HYCOM) (e.g., Chassignet et
248 al., 2009). Sea levels observed by tide gauges are important data to validate ocean circulation
249 models. Previously TBCOM used sea level data obtained at several coastal tide gauges and
250 velocity profiles from a station within the main shipping channel to evaluate the model
251 simulations (Chen et al., 2018, 2019). The veracity of TBCOM was demonstrated by simulating
252 the Tampa Bay circulation as driven by tides, winds and rivers, and reproducing the sea level and
253 circulation under both normal weather conditions (Zhu et al., 2015; Chen et al., 2019) and
254 extreme events such as Hurricane Irma (Chen et al., 2018). Similar misfits of sea levels between
255 lowpass filtered observations and model simulations were found at the tide gauge and GPS spar-
256 buoy locations (Figure 7c). These errors originate both from the open boundary sea levels that
257 propagate to the coastal and estuary areas and errors in the local winds used to force the model

(e.g., He et al., 2002; Mayer et al., 2017). Because the misfit at GPS spar-buoy station is at similar level compared to the conventional tide gauges, data obtained by the GPS spar-buoy can be used to adjust the model simulations with similar accuracy compared to a conventional tide gauge. By adjusting the simulated sea levels using the GPS spar-buoy-measured sea levels, the root mean square errors (RMSEs) between the observations and model simulations at all tide gauges were reduced by 23%-29%, and the correlation coefficients were increased by 4%-11% (Table 1).

For the diurnal to semi-diurnal tidal constituents, our TBCOM simulations clearly reveal a time lag of sea level variations at the GPS spar-buoy and the nearby tide gauge at Port Manatee (Figure 7b), consistent with the tidal harmonic analysis (Figure 4).

5 Conclusions

An anchored GPS spar-buoy system, originally designed for measuring three-component seafloor motion in shallow water, is used to measure offshore sea levels in Tampa Bay by a combination of precise positioning and GPS interferometric reflectometry. Compared to a stationary GPS site on land, this system has broader sensing zones of the reflecting surface. For individual water level retrievals, agreement between the GPS spar-buoy and a nearby acoustic tide gauge is at ~16 cm level. Harmonic analyses of the water levels measured by the GPS spar-buoy and a nearby tide gauge suggest that the amplitude differences of major tidal constituents at the two locations are no more than 1.5 cm, and the largest short period tidal height variations (diurnal and semi-diurnal) at the tide gauge lag behind the spar-buoy site by ~1.5 hr. During a 2-year period, RMS of the daily mean sea level differences measured by the two techniques is 3.1

cm. Numerical modeling of the ocean circulation throughout Tampa Bay suggest that including the offshore sea levels measured by the GPS spar-buoy can help the model to correct low-frequency sea level error propagated from the open boundary. The capabilities of measuring both seafloor motion and sea level change make the anchored GPS spar-buoy a comprehensive monitoring system.

Acknowledgments

This research was inspired by early discussions of expanding applications of the GPS spar-buoy system between SX and THD, and boosted by MAZ's suggestion of using GPS-IR for water level measurements in coastal areas. SX is supported by the Scripps Postdoctoral Scholar Award. Development of the GPS spar-buoy system was funded by U.S. NSF-OTIC grant 1538179 to THD. We acknowledge the technical support by Jason Law at the USF-CMS Ocean Circulation Group and Chad Lembke and Randy Russell at the USF-CMS Center for Ocean Technology. Tidal harmonic analyses were performed using the UTide (Codiga, 2011). Water level data measured by the tide gauge at Port Manatee, FL (NOAA station ID: 8726384) were downloaded from NOAA Tides and Currents (https://tidesandcurrents.noaa.gov/waterlevels.html?id=8726384). GPS data are archived at UNAVCO (https://doi.org/10.7283/TM3V-P845). This research was supported in part through a cooperative agreement between NOAA's Office of Coast Survey and the University of South Florida through the Center for Ocean Mapping and Innovative Technologies (COMIT), NA20NOS4000227.

References

Bevis, M., Businger, S., Herring, T.A., Rocken, C., Anthes, R.A. & Ware, R.H. (1992). GPS meteorology: Remote sensing of atmospheric water vapor using the Global Positioning System. Journal of Geophysical Research: Atmospheres, 97(D14), 15787-15801.

Chassignet, E.P, Hurlburt, H.E., Metzger, E.J., Smedstad, O.M., Cummings, J., Halliwell, G.R., Bleck, R., Baraille, R., Wallcraft, A.J., Lozano, C., Tolman, H., Srinivasan, A., Hankin, S., Cornillon, P., Weisberg, R., Barth, A., He, R., Werner, C. & Wilkin J. (2009), U.S. GODAE: Global Ocean Prediction with the HYbrid Coordinate Ocean Model (HYCOM) Oceanography, 22, 48-59.

Chen, C.S., Liu, H. & Beardsley, R.C. (2003), An unstructured, finite-volume, three-dimensional, primitive equation ocean model: Application to coastal ocean and estuaries, J. Atmos. Oceanic Technol., 20, 159–186.

Chen, J., Weisberg, R. H., Liu, Y., & Zheng, L. (2018). The Tampa Bay coastal ocean model performance for Hurricane Irma. Marine Technology Society Journal, 52(3), 33–42.

Chen, J., Weisberg, R. H., Liu, Y., Zheng, L., & Zhu, J. (2019). On the momentum balance of Tampa Bay. Journal of Geophysical Research: Oceans, 124, 4492–4510.

Codiga, D.L. (2011). Unified Tidal Analysis and Prediction Using the UTide Matlab Functions. Technical Report 2011-01. Graduate School of Oceanography, University of Rhode Island, Narragansett, RI. 59pp.

Dixon, T.H. (1991). An introduction to the global positioning system and some geological applications. Reviews of Geophysics, 29(2), 249–276.

Egbert, G.D. & Erofeeva, S.Y. (2002). Efficient inverse modeling of barotropic ocean tides. Journal of Atmospheric and Oceanic Technology 19(2), 183-204.

He, R., Liu, Y., & Weisberg, R.H. (2004). Coastal ocean wind fields gauged against the performance of a coastal ocean circulation model, Geophys. Res. Lett., 31, L14303, doi:10.1029/2003GL019261.

Ho, C.M., Mannucci, A.J., Lindqwister, U.J., Pi, X. & Tsurutani, B.T. (1996). Global ionosphere perturbations monitored by the worldwide GPS network. Geophysical Research Letters, 23(22), 3219-3222.

Karegar, M.A., Larson, K.M., Kusche, J. & Dixon, T.H. (2020). Novel quantification of shallow sediment compaction by GPS interferometric reflectometry and implications for flood susceptibility. Geophysical Research Letters, 47(14), e2020GL087807.

Landskron, D. & Böhm, J. (2018). VMF3/GPT3: refined discrete and empirical troposphere mapping functions. J Geod 92, 349–360.

Larson, K.M. (2013). A new way to detect volcanic plumes. Geophysical Research Letters, 40(11), 2657-2660.

Larson, K.M., Ray, R.D., Nievinski, F.G. & Freymueller, J.T. (2013). The accidental tide gauge: a GPS reflection case study from Kachemak Bay, Alaska. IEEE Geoscience and Remote Sensing Letters, 10(5), 1200-1204.

Larson, K.M. & Nievinski, F.G. (2013). GPS snow sensing: results from the EarthScope Plate Boundary Observatory. GPS solutions, 17(1), 41-52.

Larson, K.M., Ray, R.D. & Williams, S.D. (2017). A 10-year comparison of water levels measured with a geodetic GPS receiver versus a conventional tide gauge. Journal of Atmospheric and Oceanic Technology, 34(2), 295-307.

Larson, K.M., Lay, T., Yamazaki, Y., Cheung, K.F., Ye, L., Williams, S.D. & Davis, J.L. (2021). Dynamic Sea Level Variation from GNSS: 2020 Shumagin Earthquake Tsunami Resonance and Hurricane Laura. Geophysical Research Letters, e2020GL091378.

Liu, L. & Larson, K.M. (2018). Decadal changes of surface elevation over permafrost area estimated using reflected GPS signals. Cryosphere, 12(2).

Mayer, D.A., Weisberg, R.H., Zheng, L. & Liu, Y. (2017). Winds on the West Florida Shelf: Regional comparisons between observations and model estimates. Journal of Geophysical Research: Oceans, 122(2), 834-846, doi:10.1002/2016JC012112.

Míguez, B.M., Testut, L. & Wöppelmann, G. (2012). Performance of modern tide gauges: towards mm-level accuracy. Scientia Marina, 76(S1), 221-228.

Peng, D., Hill, E.M., Li, L., Switzer, A.D. & Larson, K.M. (2019). Application of GNSS interferometric reflectometry for detecting storm surges. GPS Solutions, 23(2), 47.

Purnell, D., Gomez, N., Chan, N.H., Strandberg, J., Holland, D.M. & Hobiger, T. (2020). Quantifying the Uncertainty in Ground-Based GNSS-Reflectometry Sea Level Measurements. IEEE Journal of Selected Topics in Applied Earth Observations and Remote Sensing, 13, 4419-4428.

Roggenbuck, O. & Reinking, J. (2019). Sea surface heights retrieval from ship-based measurements assisted by GNSS signal reflections. Marine Geodesy, 42(1), 1-24.

Roesler, C. & Larson, K.M. (2018). Software tools for GNSS interferometric reflectometry (GNSS-IR). GPS Solutions, 22(3), 1-10.

Tamisiea, M.E., Hughes, C.W., Williams, S.D. & Bingley, R.M. (2014). Sea level: measuring the bounding surfaces of the ocean. Philosophical Transactions of the Royal Society A: Mathematical, Physical and Engineering Sciences, 372(2025), p.20130336.

Wang, X., Zhang, S., Wang, L., He, X. & Zhang, Q. (2020). Analysis and combination of multi-GNSS snow depth retrievals in multipath reflectometry. GPS Solutions, 24, 1-13.

Watson, C., Coleman, R. & Handsworth, R. (2008). Coastal tide gauge calibration: a case study at Macquarie Island using GPS buoy techniques. Journal of Coastal Research, 24(4 (244)), 1071-1079.

Weisberg, R.H., Zheng, L. & Peebles, E. (2014). Gag grouper larvae pathways on the West Florida Shelf. Cont. Shelf Res., 88:11-23. doi: https://doi.org/10.1016/j.csr.2014.06.003

Williams, S.D.P. & Nievinski, F.G. (2017). Tropospheric delays in ground-based GNSS multipath reflectometry—Experimental evidence from coastal sites. Journal of Geophysical Research: Solid Earth, 122(3), 2310-2327.

Xie, S., Law, J., Russell, R., Dixon, T.H., Lembke, C., Malservisi, R., Rodgers, M., Iannaccone, G., Guardato, S., Naar, D.F., Calore, D., Fraticelli, N., Brizzolara, J., Gray, J.W., Hommeyer,

M. & Chen, J. (2019). Seafloor geodesy in shallow water with GPS on an anchored spar buoy. Journal of Geophysical Research: Solid Earth, 124(11), 12116-12140.

Zheng, L. & Weisberg R.H. (2012), Modeling the west Florida coastal ocean by downscaling from the deep ocean, across the continental shelf and into the estuaries, Ocean Modell., 48, 10–29, doi:10.1016/j.ocemod.2012.02.002.

Zhang, S., E, D., Wang, Z., Li, Y., Jin, B. & Zhou, C. (2008). Ice velocity from static GPS observations along the transect from Zhongshan station to Dome A, East Antarctica. Annals of Glaciology, 48, 113-118.

Zhu, J., Weisberg, R.H., Zheng, L. & Han, S. (2015). Influences of channel deepening and widening on the tidal and nontidal circulations of Tampa Bay. Estuaries and Coasts, 38(1), 132-150, doi:10.1007/s12237-014-9815-4.

Table 1. Correlation coefficient (CC) and root mean square error (RMSE) between observations and TBCOM simulations before and after adjusted by water levels measured with the GPS spar-buoy. Model domain, GPS spar-buoy and tide gauge locations are shown in Figure 7a.

Location	Before adjustment		After adjustment	
	CC	RMSE (cm)	CC	RMSE (cm)
Clearwater	0.90	12.5	0.94	9.5
Mckay Bay	0.86	12.2	0.93	8.9
St Petersburg	0.86	13.0	0.93	9.4
Port Manatee	0.86	14.5	0.93	11.2
GPS spar-buoy	0.84	12.5	0.93	8.8

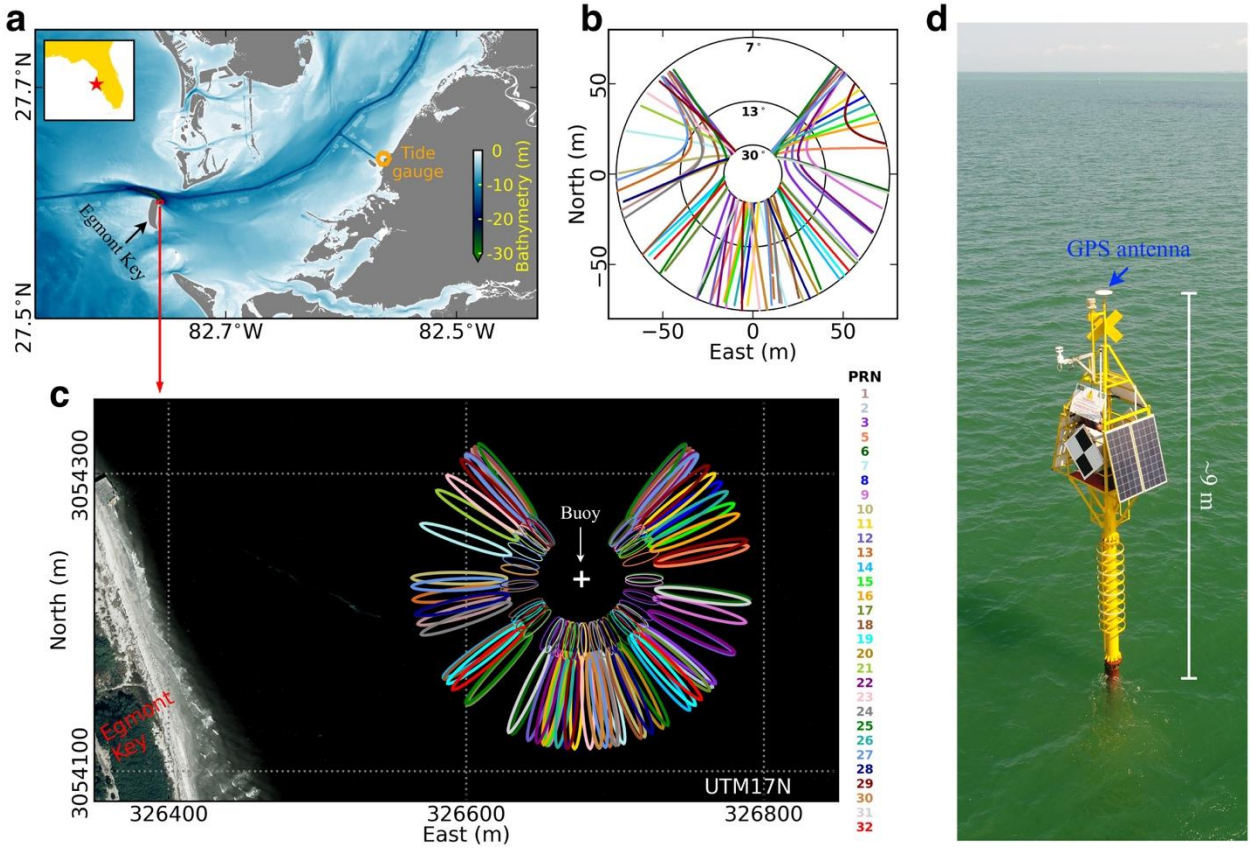

Figure 1. Study area and GPS spar-buoy system. (a) Location of the study area, distance between the buoy and a conventional tide gauge (orange hexagon) is 19.5 km. (b) GPS-signal multipath reflection points on 6 June 2019 when satellite elevation angles are between 7º and 30º, colors correspond to different GPS satellites labeled by pseudorandom noise (PRN) codes in c. (c) Sensing zones (first Fresnel zones) for satellites at 7º (thick line ellipses) and 13º (thin line ellipses) elevation angles on 6 June 2019. (d) The above-waterline portion of the GPS spar-buoy system.

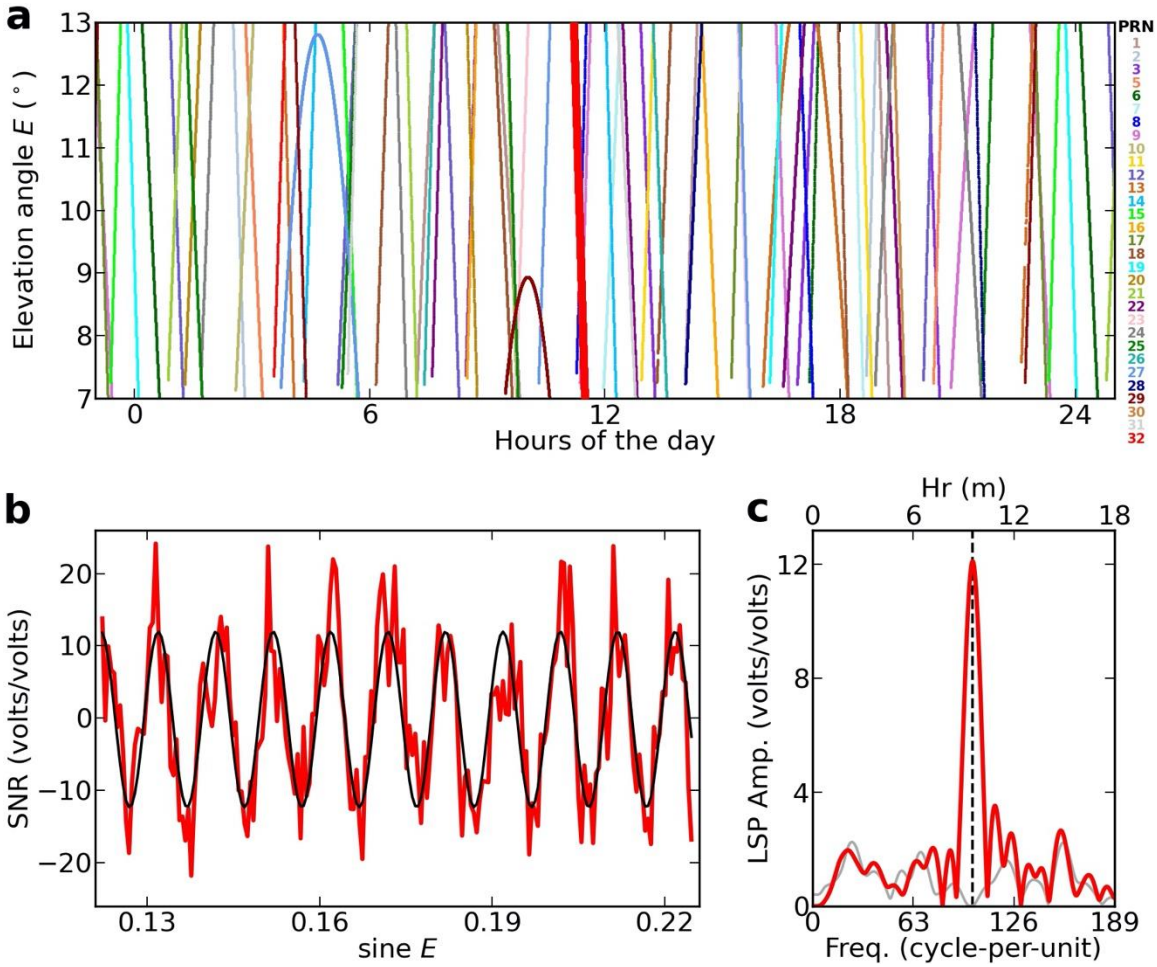

Figure 2. An example of using GPS interferometric reflectometry to retrieve water level. (a) GPS satellites observed by the receiver at elevation angles between 7º-13º on 6 June 2019. (b) Signal-to-noise ratio (SNR) data for the descending track of satellite PRN 32 (marked by the thick red line in a). Red line shows the detrended SNR data, black line shows the least squares fitting of a sine function. (c) Lomb-Scargle periodogram (LSP) of the detrended SNR data, frequencies are converted to GPS heights above the reflecting surface. Red line shows LSP for the data shown by red line in b. Grey line shows the LSP for data with peak frequency signal (black line in b) subtracted.

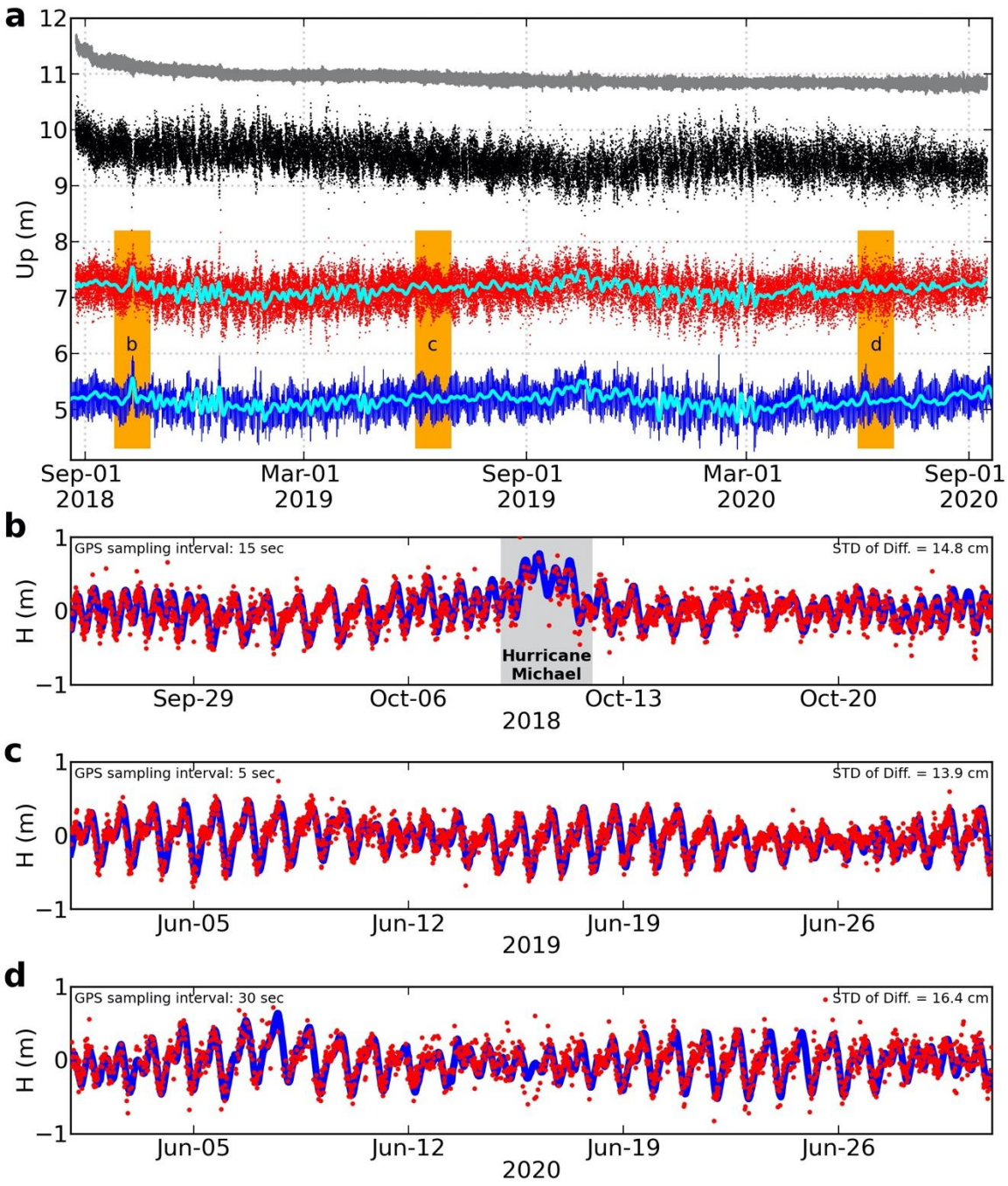

Figure 3. GPS spar-buoy and tide gauge observed water levels. (a) Grey dots show GPS antenna vertical displacements. Black dots show GPS-IR estimated reflecting heights. Red dots show the GPS spar-buoy derived water levels. Blue line shows tide gauge observed water levels (tide gauge location is shown in Figure 1a). Cyan lines show 0.2 cycle-per-day low-frequency-pass filtered water levels. Note except for the black dots, all other markers are offset for clarity. (b-d) Zoom in view of the GPS spar-buoy and tide gauge observed water levels for periods marked by orange color in a. Blue for the tide gauge, red for the GPS spar-buoy. Standard deviation (STD) of the differences is annotated on the upper right.

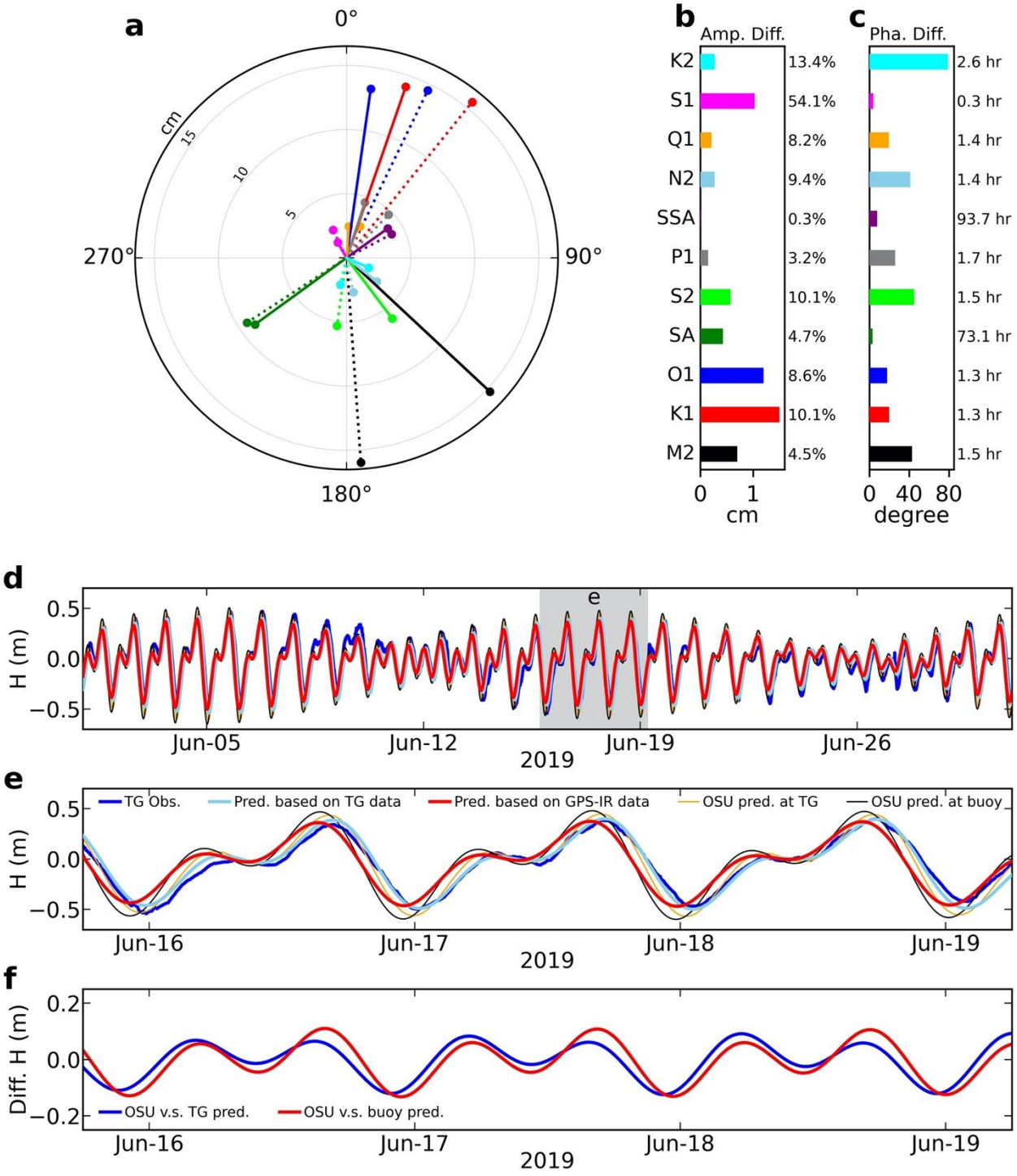

Figure 4. Tidal analyses and predictions. (a) The eleven largest tidal constituents from harmonic analyses of the tide gauge (dotted line) and GPS spar-buoy (solid line) observations, plotted in polar projection. Each color corresponds to a tidal constituent shown in b and c with the same color. (b) Amplitude differences of tidal constituents between the tide gauge and GPS spar-buoy derived results, bottom to top corresponds the largest to smallest tidal constituent (M2 to K2), the

441 right annotations are percentages of the amplitude difference in the amplitude (average of the
442 amplitudes from the two techniques). (c) Phase differences of tidal constituents between the tide
443 gauge and GPS spar-buoy derived results. The corresponding time lags are annotated on the right.
444 (d, e) Water level predictions. Blue line shows tide gauge observed water levels for comparison.
445 (f) Difference in sea level predictions based on observations and model. TG – tide gauge, OSU –
446 OSU TPXO model (Egbert & Erofeeva, 2002).
447

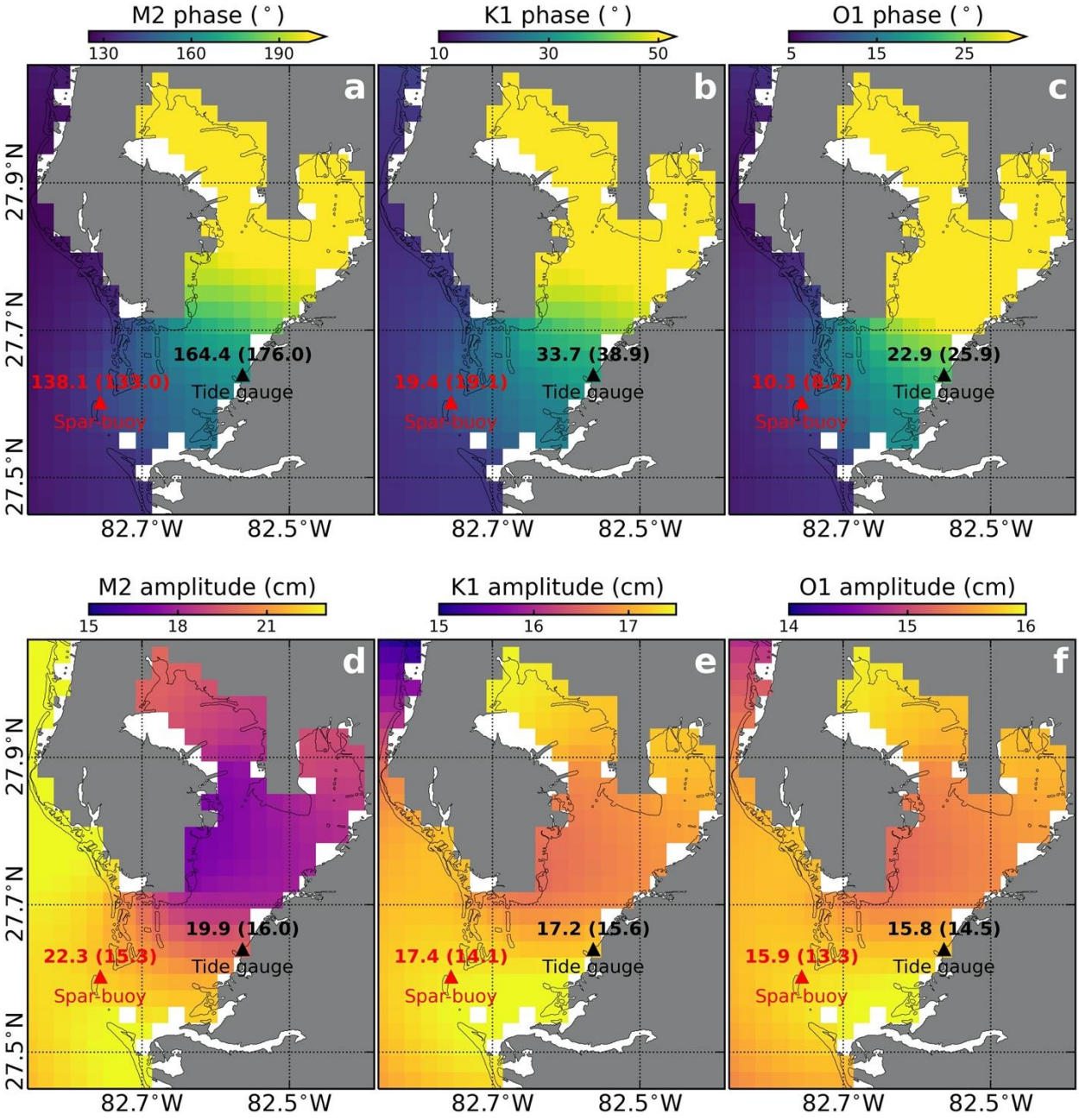

Figure 5. Comparison of the phase (top) and amplitude (bottom) of the largest three tidal constituents observed at the spar-buoy and the tide gauge locations. Color maps show OSU TPXO regional tidal solutions for the Gulf of Mexico. Phase (º) or amplitude (cm) at the spar-buoy or tide gauge location is annotated above corresponding triangle marker, with OSU TPXO modeled value first and then result derived from the GPS spar-buoy or tide gauge observations (in parentheses).

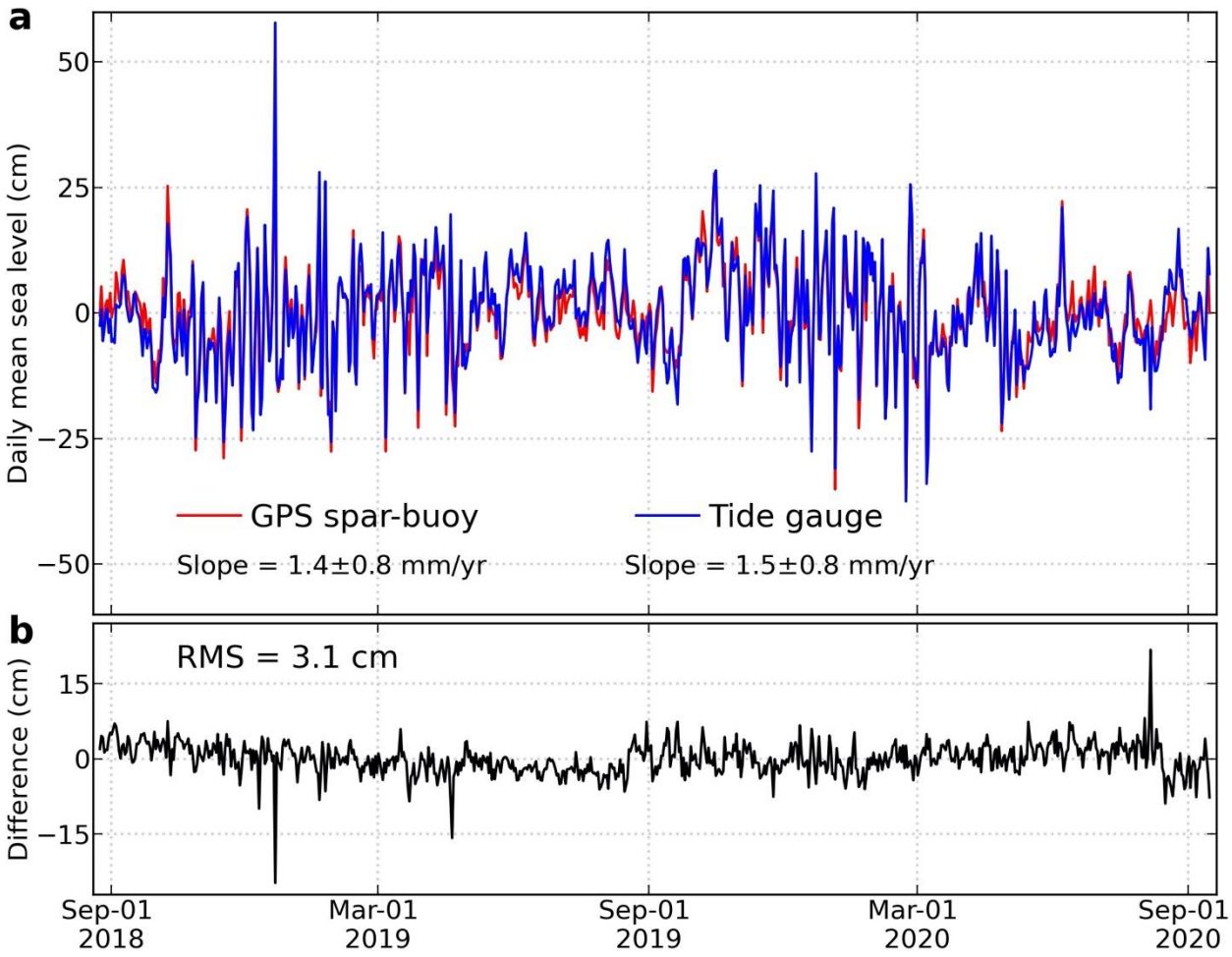

Figure 6. Comparison of de-tided daily mean sea levels measured by the GPS spar-buoy and tide gauge.

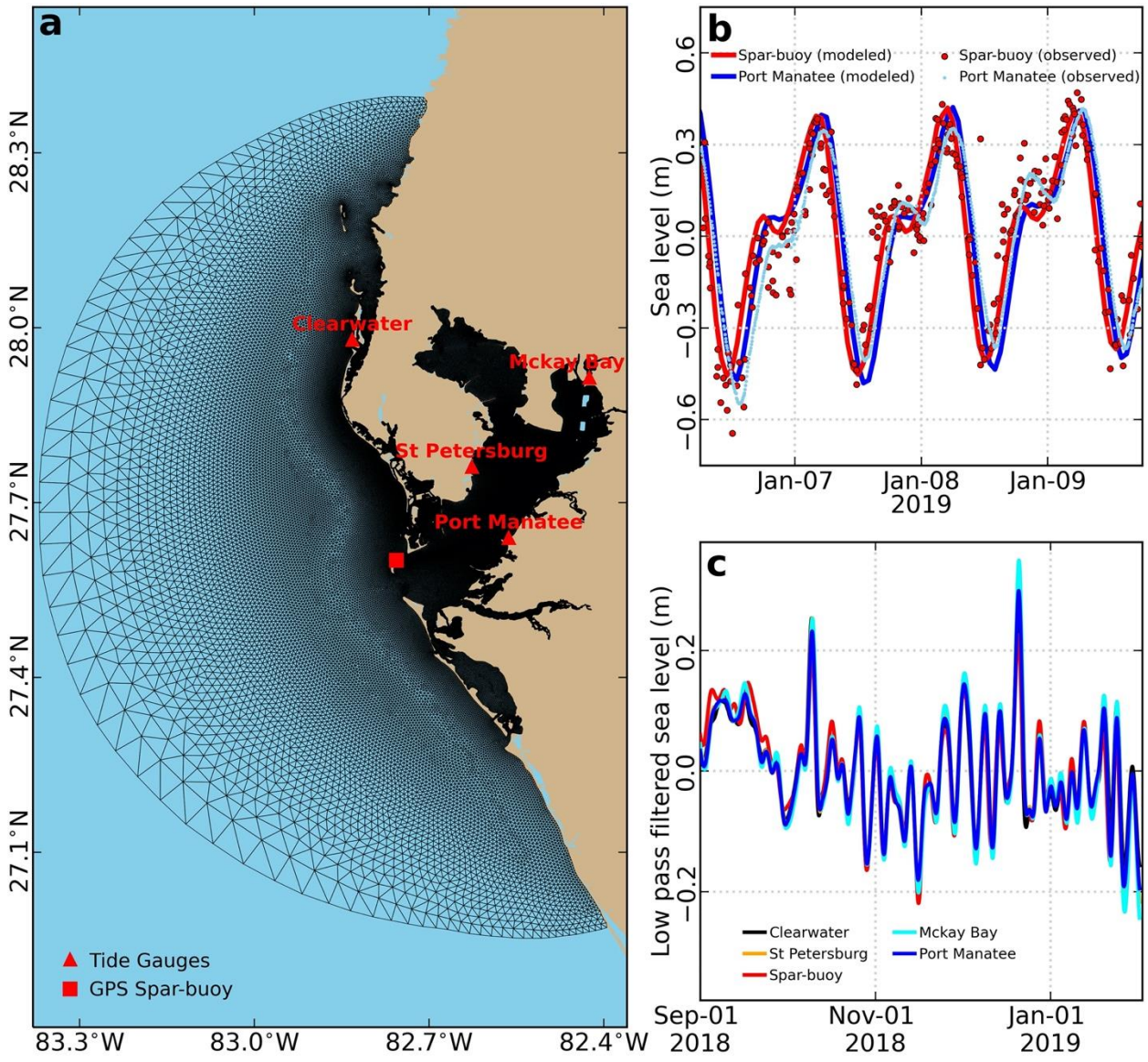

Figure 7. Sea levels modeled by the Tampa Bay Coastal Ocean Model (TBCOM). (a) Black mesh shows the model domain, red markers mark the GPS spar-buoy and tide gauge locations. (b) 3.5-day example of observed and hourly modeled sea levels at the GPS spar-buoy and the Port Manatee tide gauge. (c) Differences between the low pass filtered observed and model simulated sea levels at the GPS spar-buoy and tide gauges. Details of the TBCOM modeling scheme were described in Chen et al. (2018, 2019).